



Effect of Stenosis Severity on Wall Shear Stress Based Hemodynamic Descriptors using Multiphase Mixture Theory

A. Buradi and A. Mahalingam[†]

Multiphase Fluid Dynamics Laboratory, Department of Mechanical Engineering, National Institute of Technology Karnataka Surathkal, P.O. Srinivasnagar - 575025, Mangalore, D.K., Karnataka State, India

[†] Email: m.arun1978@gmail.com

(Received April 3, 2018; accepted June 16, 2018)

ABSTRACT

A variety of wall shear stress (WSS) based hemodynamic descriptors have been defined over the years to study hemodynamic flow instabilities as potential indicators or prognosticators of endothelial wall dysfunction. Generally, these hemodynamic indicators have been calculated numerically using ‘single phase’ approach. In single phase models, the flow-dependent cell interactions and their transport are usually neglected by treating blood as a single phase non-Newtonian fluid. In the present investigation, a multiphase mixture-theory model is used to define the motion of red blood cells (RBCs) in blood plasma and interactions between these two-components. The multiphase mixture theory model exhibited good agreement with the experimental results and performed better than non-Newtonian single phase model. The mixture-theory model is then applied to simulate pulsatile blood flow through four idealized coronary artery models having different degrees of stenosis (DOS) severities viz., 30, 50, 70 and 85% diameter reduction stenosis. The maximum WSS is seen at the stenosis throat in all the cases and maximum oscillatory shear index (OSI) is seen in downstream region of the stenosis. Our findings suggest that for degree of coronary stenosis more than 50%, a more disturbed fluid dynamics is observed downstream of stenosis. This could lead to further progression of stenosis and may promote a higher risk of atherogenesis and plaque buildup in the flow-disturbed area. The potential atherosclerotic lesion sites were identified based on clinically relevant values of WSS, time-averaged WSS gradient (TAWSSG), time-averaged WSS (TAWSS), and OSI. Finally, the change in potential atherosclerotic lesion sites with respect to DOS has been quantified.

Keywords: Multiphase mixture model; Computational fluid dynamics; Stenosis; Wall shear stress; Coronary artery; Oscillatory shear index.

1. INTRODUCTION

Atherosclerosis is considered to be an endothelial disease which is generally found in medium and large sized arteries. This causes the narrowing of arteries which hinders the blood flow to the tissues (Nichols and O'Rourke 2005). In coronary arteries, the hemodynamic changes due to the presence of plaque buildup are correlated with higher risk of adverse clinical outcome. One substantial implication revealed from recent studies (Malek *et al.* 1999; Chatzizisis *et al.* 2007) states that regional wall shear stress (WSS) plays a key and fundamental role in the localization of atherosclerosis and in particular, low and oscillatory WSS (0.5 Pa) has been correlated to region of localization of atherosclerosis and the magnitude of low WSS been associated with the severity of atherosclerosis.

Oscillatory shear index (OSI) which is another WSS based hemodynamics parameter is used as a predictor for the atherosclerosis plaque formation and susceptibility of plaque in coronary arteries (Zhang *et al.* 2008; Ryou *et al.* 2012). High OSI value is strongly related to the development of atherosclerosis since it affects the endothelial cells arrangement in adjacent tissues. Also, high OSI value regions are generally located in the low WSS regions [Stadler *et al.* 1990; Ryou *et al.* 2012].

Hitherto, most of the hemodynamics studies have used computational fluid dynamics (CFD) techniques to better understand the various hemodynamic descriptors by considering blood as a single-phase Newtonian (He and Ku 1996; Berthier *et al.* 2002; Zeng *et al.* 2003; Hoi *et al.* 2004; Hasan and Das 2008; Aayani *et al.* 2016; Mesri *et al.* 2017) and non-Newtonian fluid (Gijzen *et al.* 1999; Steinman 2002; Razavi *et al.* 2011; Li *et al.* 2015;

Yan *et al.* 2017). However, the blood is intrinsically a suspension of RBCs, WBCs, platelets and other lipoproteins in blood plasma. Several experimental studies (Haynes 1960; Reinke *et al.* 1987; Stadler *et al.* 1990; Egorov *et al.* 1994) have observed the dense granular nature of blood and its heterogeneous distribution and concluded that simulation of blood requires a multiphase approach/model to explain clearly the interaction of blood particulates with the lumen surface and its complex behavior. In single-phase studies, the details of blood cells transport and their interactions with varying percentage of stenosis severities were missing. Therefore, a good multiphase approach considering the blood cell transport and their interactions is essential for better understanding the underlying pathology and pathological development of coronary artery disease (CAD).

A large number of research articles have been published typically wherein one of the two multi-component theories: the Mixture Theory (Rajagopal *et al.* 1992) and averaging methods (Ishii and Hibiki 2010) have been used. The approach of both theories is based on an assumption that each phase may be represented mathematically as a continuum (Kizilova *et al.* 2012). Although the approaches of both the theories look similar, their formulations of constitutive models are completely different. Indeed, many researchers have been reported that the interaction models used in averaging methods are not frame-indifferent, hence it violating the fundamentals of physics as revealed by Massoudi (Massoudi 2002). Generally, the drag models used along with the averaging methods holds good only for fluid particles or solid spherical particles which are in low concentration and sufficiently small in size. Hence, in this study, we use the theory of interacting continua or mixture theory to model the blood consisting of two-phase mixture (i.e., plasma and RBCs).

The effects of the platelets, WBCs and other components in the blood are neglected owing to their negligible volume concentration. The effect of mass or biochemical inter conversions are not considered in this study. The RBC's volume fraction is considered as a scalar field variable. In addition, we assumed that the plasma acts as a Newtonian fluid and RBCs were considered as solid spherical particles with its viscosity dependent on the hematocrit and local shear rate. Plasma-RBC interaction forces are considered by implementing the drag and lift forces.

To date, according to the best knowledge of the authors, only limited research has been done on studying clinically relevant WSS based

hemodynamic indicators considering blood as multi-component fluid and there is no published data on the effect of stenosis severity in the coronary artery considering blood as multiphase fluid. Hence, the present computational study was set up to assess the influence of different degrees of stenosis (DOS) severities such as 30%, 50%, 70% and 85% stenosis on WSS based hemodynamic parameters such as TAWSS, TAWSSG and OSI using multiphase approach. Finally, the relationships between the bulk flow hemodynamics and various WSS-based-hemodynamic descriptors have been established. The current multiphase mixture model has been compared with single phase model and validated with experimental studies.

2. MATERIALS AND METHODS

2.1 Geometry Representation and Computational Mesh Generation

In the present multiphase blood flow modelling an ideal arterial geometry model with varying DOS severity has been considered. Figure 1 shows the blood vessel model (with dimensions) including its stenosis as a three-dimensional (3D) axisymmetric straight tube for the numerical blood flow analysis. The geometry of stenosis is defined by the cosine function:

$$\frac{r(x)}{R} = 1 - \delta_c \left[1 + \cos\left(\frac{x\pi}{D}\right) \right], -D \leq x \leq D \quad (1)$$

Where, x and r are the axial and radial coordinates, respectively. R and D , respectively correspond to the radius and diameter of un-stenosed vessel. The δ_c is a constant and takes the value of 0.70, 0.50, 0.30 and 0.15 resulting in 30%, 50%, 70% and 85% of diameter reduction at the stenosis throat as shown in Fig. 2. The length of the stenosed zone, inlet zone and outlet zone is 8mm (2D), 56mm (14D) and 116mm (29D), respectively and combining all lengths gives a total length of 180 mm. The selected coronary artery geometry had a 4 mm of lumen diameter which is typical of left main coronary artery (Nosovitsky *et al.* 1997).

The computer-aided design software GAMBIT 2.4.6 (FLUENT, ANSYS, Canonsburg, PA, USA) is used for the generation of 3D idealized geometries and the grid. For generation of unstructured tetrahedral mesh with variable mesh spacing a robust scheme was adapted to signify the rapidly and small varying features in the stenosis region. The final grid contains 389180 elements as shown in Fig. 3.

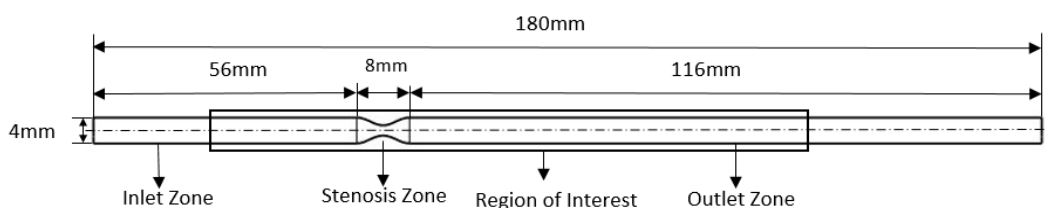


Fig. 1. Ideal stenosed vessel geometry with dimensions showing the boundary conditions and region of interest where four different stenosis geometries are simulated to demonstrate hemodynamic variations.

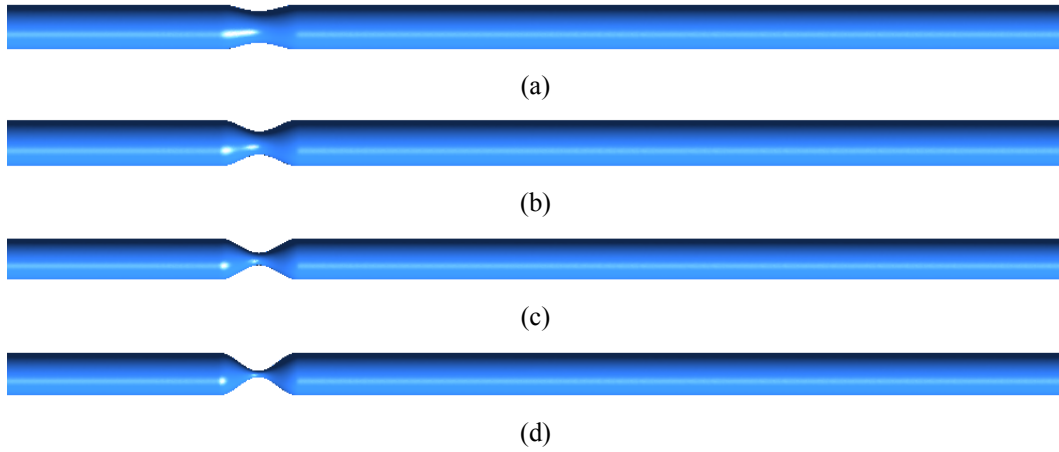


Fig. 2. Idealized stenosis vessel geometries for different DOS severity, a). 30%, b). 50%, c). 70%, and d). 85% stenosis.

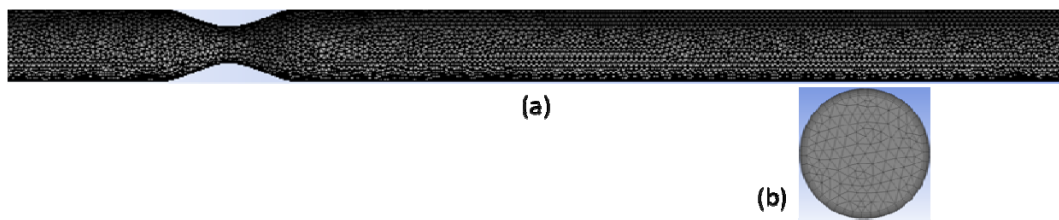


Fig. 3. Computational grid. a 3-D computational grid for idealized coronary artery with 50% diameter reduction stenosis. b Zoomed view of inlet grid presenting the prism layer to capture the flow near wall.

2.2 Multiphase Blood Flow Model

Developments in the field of CFD have imparted the basis for garnering further insight into the multiphase flow dynamics. In the present study, the theory of interacting continua is used to study the hemodynamics in an idealized coronary artery since it has better accuracy compared to the Euler-Euler method. The mixture theory model solves the conservation of mass, momentum and energy equation for the mixture. In addition, for the secondary phases it solves volume fraction (hematocrit) equations and for the relative velocities it solves the set of algebraic equations which are also presented in below.

2.2.1 Continuity Equation

Using the mixture theory model the continuity equation is given as

$$\frac{\partial}{\partial t}(\rho_m) + \nabla \cdot (\rho_m \bar{v}_m) = 0, \quad (2)$$

$$\bar{v}_m = \frac{\sum_{k=1}^n \epsilon_k \rho_k \bar{v}_k}{\rho_m}, \quad (3)$$

$$\rho_m = \sum_{k=1}^n \epsilon_k \rho_k, \quad (4)$$

Where, \bar{v}_m , ρ_m and ϵ_k correspond to the mass-averaged velocity, mixture density and the

hematocrit of phase ‘k’ respectively.

For different phases, the sum of all the hematocrits must be equal to 1:

$$\sum_{k=1}^n \rho_k \epsilon_k = 1 \quad (5)$$

2.2.2 Momentum Equation

The summation of individual momentum equations for all the phases is used to obtain the momentum equation for the mixture “Eq. (6)”.

$$\begin{aligned} \frac{\partial}{\partial t}(\rho_m \bar{v}_m) + \nabla \cdot (\rho_m \bar{v}_m \bar{v}_m) = -\nabla P \\ + \nabla \cdot [\mu_m (\nabla \bar{v}_m + \nabla \bar{v}_m^T)] + \rho_m \bar{g} \\ + \bar{F} - \nabla \cdot \left(\sum_{k=1}^n \epsilon_k \rho_k \bar{v}_{dr,k} \bar{v}_{dr,k} \right) \end{aligned} \quad (6)$$

Where, n , \bar{F} and μ_m correspond to the number of phases, body force and the mixture viscosity, respectively. The μ_m expressed as:

$$\mu_m = \sum_{k=1}^n \epsilon_k \mu_k \quad (7)$$

And $\bar{v}_{dr,k}$ - secondary phase (k) drift velocity:

$$\bar{v}_{dr,k} = \bar{v}_k - \bar{v}_m \quad (8)$$

The drift velocity is active when any one of the two phases is present in particle form. Due to the minimal influence of buoyancy force and external force (rotational, shear lift, and virtual mass) on blood they are neglected in momentum equations.

2.2.3 Slip and Drift Velocity

The secondary phase (p) velocity relative to the primary phase velocity (q) is called as the slip velocity. It is expressed as:

$$\vec{v}_{pq} = \vec{v}_p - \vec{v}_q \quad (9)$$

Also, for any phase (k) the mass fraction (C_k) is expressed as:

$$C_k = \frac{\varepsilon_k \rho_k}{\rho_m} \quad (10)$$

\vec{v}_{pq} and $\vec{v}_{dr,p}$ are related by the following equation:

$$\vec{v}_{dr,p} = \vec{v}_{pq} - \sum_{k=1}^n C_k \vec{v}_{qk} \quad (11)$$

The relative velocity (\vec{v}_{pq}) is given by (Manninen *et al.* 1996),

$$\vec{v}_{pq} = \frac{\tau_p (\rho_p - \rho_m)}{f_d} \vec{a} \quad (12)$$

Where τ_p represents the relaxation time of particle

$$\tau_p = \frac{\rho_p d_p^2}{18\mu_q} \quad (13)$$

Where, d_p and \vec{a} , respectively correspond to the diameter and acceleration of secondary phase particles and f_d is the drag force applied by the fluid on spherical particles. For the two phases, an interphase drag term is added to consider the exerted force of drag by fluid on spherical rigid particles. For the force of drag, between RBCs and plasma, the Gidaspow model (Gidaspow 1994) was embraced to validate the densely distributed RBCs.

The drag force term is expressed as

$$f_{d(rbc, plasma)} = C_{rbc} (\mathbf{u}_{rbc} - \mathbf{u}_{plasma}) \quad (14)$$

Where \mathbf{u}_{plasma} and \mathbf{u}_{rbc} , respectively correspond to the plasma and RBCs phase velocity, C_{rbc} denotes the momentum exchange coefficient between phases, is given by:

$$C_{rbc} = \frac{3 C_D}{4 d_{rbc}} \varepsilon_{rbc} \varepsilon_{plasma} \rho_{plasma} |\mathbf{u}_{rbc} - \mathbf{u}_{plasma}| \quad (15)$$

Where d_{rbc} is the diameter of RBC i.e. 8 μm . For both dilute and dense particles, the Gidaspow model (Gidaspow 1994) assumes two different systems of equations for drag coefficient.

For, $\varepsilon_{rbc} < 0.2$, C_D is defined as

$$C_D = \varepsilon_{rbc}^{-1.65} \max \left(\frac{24}{\text{Re}'_p} (1 + 0.15 \text{Re}'_p{}^{0.687}), 0.44 \right) \quad (16)$$

Where, Re'_p represents the modified Reynolds number of particle and represented as:

$$\text{Re}'_p = \frac{\rho_{plasma} \varepsilon_{plasma} d_{rbc} |\mathbf{u}_{rbc} - \mathbf{u}_{plasma}|}{\mu_{plasma}} \quad (17)$$

For $\varepsilon_{rbc} > 0.2$, the momentum exchange coefficient between phases (C_{rbc}) is directly expressed as:

$$C_{rbc} = 150 \frac{(1 - \varepsilon_{rbc})^2 \mu_{plasma}}{\varepsilon_{rbc} d_{rbc}^2} + 1.35 \frac{(1 - \varepsilon_{rbc}) \rho_{plasma} |\mathbf{u}_{rbc} - \mathbf{u}_{plasma}|}{d_{rbc}} \quad (18)$$

2.2.4 Constitutive Model

The strain rate tensor $\underline{\underline{\dot{\gamma}}}$ and viscous stress tensor $\underline{\underline{\tau}}$ are considered to represent the constitutive model. It is expressed as:

$$\underline{\underline{\dot{\gamma}}} = \nabla \vec{v} + (\nabla \vec{v})^T \quad (19)$$

The significance of $\underline{\underline{\dot{\gamma}}}$ and $\underline{\underline{\tau}}$, are expressed by $\dot{\gamma}$ and τ , respectively and is expressed s:

$$\dot{\gamma} = \sqrt{\frac{1}{2} \text{II} \dot{\underline{\underline{\dot{\gamma}}}}} = \sqrt{\frac{1}{2} \dot{\underline{\underline{\dot{\gamma}}}} : \dot{\underline{\underline{\dot{\gamma}}}}} \quad (20)$$

$$\tau = \sqrt{\frac{1}{2} \text{II} \underline{\underline{\tau}}} = \sqrt{\frac{1}{2} \underline{\underline{\tau}} : \underline{\underline{\tau}}} \quad (21)$$

Where, $\nabla \vec{v}$, \vec{v} and II is respectively denotes the velocity-gradient tensor, velocity vector and second invariant of a stress tensor, whereas, the superscript T represents its transpose. For the viscous fluid the constitutive behavior is expressed by

$$\underline{\underline{\tau}} = \mu \underline{\underline{\dot{\gamma}}} \quad (22)$$

Where, μ is the dynamic viscosity of blood.

In general, the rheological properties of blood are complex in small arteries because of its strong non-Newtonian behavior such as viscoelasticity, shear-thinning, and thixotropic (Oka 1981) and the time dependent viscosity of blood is determined by the

aggregation and disaggregation of particles (RBCs). In the present study, the viscosity is considered as a function of shear rate and hematocrit (Quemada 1981).

To account the blood non-Newtonian behavior, Quemada viscosity model is used in this study (Quemada 1977; Quemada 1978). Compared to the different non-Newtonian models, the Quemada viscosity model is exclusively reliant on the RBC's hematocrit and local shear rate and holds good for broader range of shear rates during each cardiac cycle from end-diastole (low shear) to peak systole (high shear). The change in RBC volume fraction cannot be calculated directly using single phase models. This is one added advantage of the present model over traditional single phase models. Also, the distribution and time evolution of RBC's is correlated to the blood flow field through dynamic shear viscosity and defined as

$$\mu = \mu(\varepsilon_{rbc}, \dot{\gamma}) = \mu_{plasma} \left[1 - \frac{1}{2} \left(k_{\infty} + \frac{k_0 - k_{\infty}}{1 + (\dot{\gamma} / \dot{\gamma}_c)^q} \right) \varepsilon_{rbc} \right]^{-2} \quad (23)$$

Where $\mu_{plasma} = 0.00132 \text{ Pa s}$ (Lowe *et al.* 1993; Caro 2012) is the plasma viscosity, q is an empirical parameter, ε_{rbc} is the RBC hematocrit and parameters k_0 , k_{∞} and $\dot{\gamma}_c$, respectively, correspond to the lower, higher and critical shear rates of non-dimensional intrinsic viscosities. Cokelet (Cokelet 1987) investigated various empirical correlations and expressed as a function of RBC hematocrit for each of these parameters, which is given by:

$$\dot{\gamma}_c(\varepsilon_{rbc}) = e^{(-6.1508 + 27.923\varepsilon_{rbc} - 25.6\varepsilon_{rbc}^2 + 3.697\varepsilon_{rbc}^3)} \quad (24)$$

$$k_0(\varepsilon_{rbc}) = e^{(3.874 - 10.41\varepsilon_{rbc} + 13.8\varepsilon_{rbc}^2 - 6.738\varepsilon_{rbc}^3)} \quad (25)$$

$$k_{\infty}(\varepsilon_{rbc}) = e^{(1.3435 - 2.803\varepsilon_{rbc} + 2.711\varepsilon_{rbc}^2 - 0.6479\varepsilon_{rbc}^3)} \quad (26)$$

2.3 Boundary Conditions

A transient simulation was carried out using fluid and rheological properties of blood. The volume inflow velocity profile were used as velocity inlet

boundary conditions obtained from Berne and Levy (Berne and Levy 1967) and shown in Fig. 4. At inlet, a fully developed time-dependent velocity profile is considered and used in ANSYS Fluent as a C language user-defined function (UDF) code and coupled to the CFD code. Maximum Reynolds numbers of 410 is attained based on artery diameter at the inlet during maximum flow at beginning of diastole. The stenosis and blood-vessels were assumed to be rigid and the flow of blood was assumed to be laminar. The outflow and no-slip conditions were applied to outlet and wall boundary conditions respectively.

2.4 Numerical Scheme

With appropriate inlet and outlet boundary conditions, an ANSYS FLUENT 14.5 [ANSYS Inc., Canonsburg, PA, USA] with multiphase mixture model was employed to solve the coupled nonlinear PDE (partial differential equation) of blood flow. For pressure-velocity coupling the coupled scheme was employed. A coupled solver with first-order and second-order upwind schemes was used for spatial discretization of volume fraction and momentum terms respectively. Figure 4 shows the pulsatile phasic inflow velocity profile used at inlet boundary conditions for plasma and RBCs. In this study, 1025 kg/m^3 and 1100 kg/m^3 were chosen as the density of plasma and RBCs respectively (Bronzino 1999; Caro 2012). At the artery inlet cross section uniform velocity profiles were maintained. The zero slip velocity was applied as wall boundary condition for both plasma and RBC's. The volume fraction of RBC is maintained steady and uniform with 45% at the inlet. The particles of RBCs were assumed to be spherical with $8\mu\text{m}$ as average diameter and a shape factor of $\phi = 1$.

The simulations were carried out with a maximum residual corresponding to the convergence flow of 10^{-3} . Also, constant time step of 0.001s was chosen with 200 iterations for each time-step. To ensure the periodicity, the simulations were carried out for four pulsatile cycles and the analysis was carried out for the third cycle. Reynolds number and Womersley parameter, respectively found to be 737 and 3.2. The mean Reynolds number (R_e) and Womersley parameter (W_0) were calculated, respectively using the equation,

$$R_e = \rho_{mix} U_0 D / \mu_{mix} \quad (27)$$

and

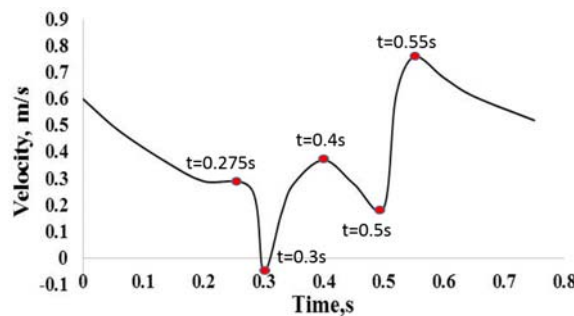


Fig. 4. Inlet pulsatile coronary velocity profile for blood (plasma and RBC) along the time of the cardiac cycle (Berne & Levy 1967). End of diastole (0.275s), reversed flow in early systole (0.30s), local maximum systole (0.4s), local minimum systole (0.5s), and maximum flow at beginning of diastole (0.55s).

$$W_0 = D / 2\sqrt{2\pi / T(\rho_{mix} / \mu_{mix})} \quad (28)$$

Where, T is the cardiac cycle time period and U_0 is the average inlet velocity (ms^{-1}).

2.5 WSS Based Hemodynamic Descriptors

The various WSS based hemodynamic descriptors are calculated by using the stated equations below. The WSS is a biomechanical parameter, producing a tangential force on the vascular endothelial cell surface and near the wall it is a function of the velocity gradient and regulates the arterial wall remodeling. The WSS is given by

$$\tau = \mu \left(\frac{\partial u}{\partial y} \right)_w \quad (29)$$

2.5.1 Time-Averaged Wall Shear Stress

It is the averaged WSS over one pulsatile cycle, used to determine the shear stress magnitude applied on the vascular wall surface during one pulsatile cycle. It is given as

$$TAWSS = \frac{1}{T} \int_0^T |WSS| dt \quad (30)$$

The value of $TAWSS < 0.4$ Pa endorses an atherogenic endothelial phenotype, whereas the values with high $TAWSS$ (15-45 Pa) are known to thrombogenic (Malek *et al.* 1999). The high values of $TAWSS$ can lead to damage of endothelial cells (Suess *et al.* 2016).

2.5.2 Time-Averaged Wall Shear Stress Gradient

It is a transient fluid flow property, correlated to the wall of the artery throughout a pulsatile cycle. Speedy changes of WSS over small spaces are measured by $TAWSSG$ and is defined as

$$TAWSSG = \frac{1}{T} \int_0^T \sqrt{\left(\frac{\partial \tau_x}{\partial x} \right)^2 + \left(\frac{\partial \tau_y}{\partial y} \right)^2 + \left(\frac{\partial \tau_z}{\partial z} \right)^2} dt \quad (31)$$

2.5.3 Oscillatory Shear Index

It is a hemodynamic descriptor used to measure the WSS directional change during one pulsatile cycle. The OSI value falls between the ranges of 0 and 0.5, corresponding to least and severe temporal shear rate conditions respectively. It is given by

$$OSI = 0.5 \times \left(1 - \frac{\int_0^T |WSS| dt}{\int_0^T |WSS| dt} \right) \quad (32)$$

OSI is generally used to describe the flow field disorder near the wall and high OSI (near 0.5) highlights the possible atherosclerosis prone regions (He and Ku 1996).

2.6 Model Validation

2.6.1 Blood Flow and Velocity Distribution Study

To demonstrate the accuracy of the multiphase mixture model, an initial blood flow simulation was performed in a rectangular microchannel (Patrick *et al.* 2011) as shown in Fig. 5 with 45% of RBCs hematocrit. The inlet velocity was given as 350 $\mu\text{m/s}$ and the inlet RBC volume fraction was 0.45. Numerical results using single phase and multiphase mixture model were obtained for RBC velocity distribution under fully developed steady flow conditions and presented in Fig. 6 along with experimental data.

From Fig. 6 it is evident that the multiphase mixture model predicted the velocity profiles at different downstream locations in the microchannel better than single phase model. Whereas there is a slight discrepancies in results between the numerical simulation and experimental data, this is mainly due to the flexibility of RBCs, wall porosity and the flexibility of blood vessels which has been ignored in the present study. The percentage error between predicted peak velocities and the experimental values is quantified in Table 1. It is observed that the percentage error in calculated maximum peak velocity reduced significantly for the multiphase model when compared error using single phase model. Hence, in the present study multiphase mixture theory model is employed for blood flow simulations in idealized stenosed coronary arteries with varying DOS severities.

2.7 Model Verification

Apart from the validation, model verification process is used to confirm the numerical results. It includes the analysis of various input parameters applied to the computational model.

2.7.1 Grid Independence Study

The grid independence study has been carried out with four tetrahedral meshes for the fluid domain geometry of the idealized coronary artery model with mesh elements 230659, 286142, 389180 and 445680. The mesh independence study was performed with steady state boundary conditions using the laminar blood flow model by monitoring the axial velocity profile of the model at different axial locations before the stenosis (i.e., 1D and 2D) as seen in Fig. 7.

It can be perceived from the axial velocity profiles plot, meshes with 286142 and 389180 elements are following the same velocity profile trend of finest mesh elements 445680. Hence, the model with 389180 mesh elements was considered for further numerical analysis which reduces the calculation time without negotiating accuracy of the results. Also, the same number of mesh elements is adopted for all stenosed artery models.

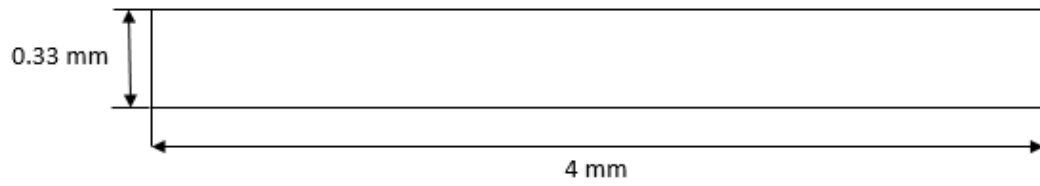


Fig. 5. Micro-channel rectangular flow system, with 100 μm depth in z-direction (Patrick *et al.* 2011).

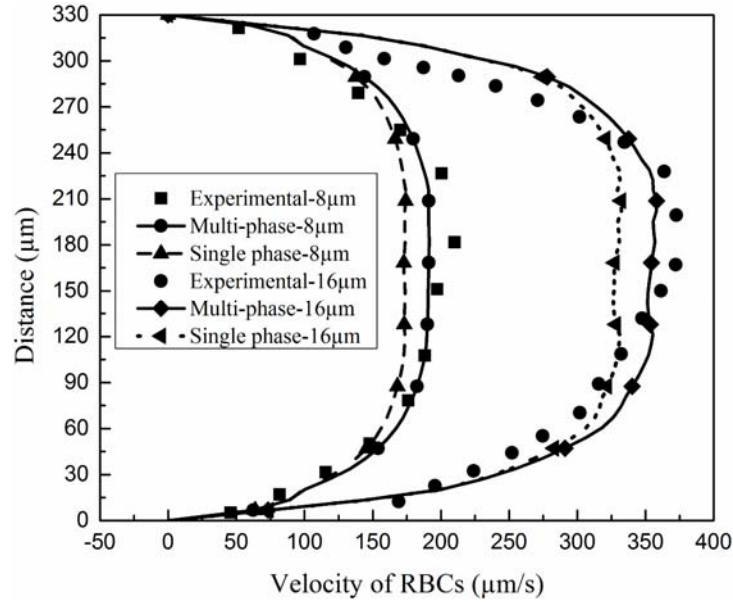


Fig. 6. Comparison of present numerical (Single phase and Multiphase) and experimental results (Patrick *et al.* 2011) of RBC velocity distribution along stream-wise direction (x) as a function of the wall distance (y) at the depths $z = 8 \mu\text{m}$ and $z = 16 \mu\text{m}$.

Table 1 Maximum peak velocity and percentage error between single phase and multiphase model compared to experimental data at the depths $z = 8 \mu\text{m}$ and $z = 16 \mu\text{m}$

| Validation study | At depth $Z=8 \mu\text{m}$ | | At depth $Z=16 \mu\text{m}$ | |
|---|--|---------|--|---------|
| | Maximum Peak Velocity in $\mu\text{m/s}$ | % Error | Maximum Peak Velocity in $\mu\text{m/s}$ | % Error |
| Experimental (Patrick <i>et al.</i> 2011) | 209.92 | - | 373.03 | - |
| Single-Phase Model | 147.16 | -17.03 | 332.18 | -10.95 |
| Multi-phase Model | 191.36 | -8.84 | 358.10 | -4 |

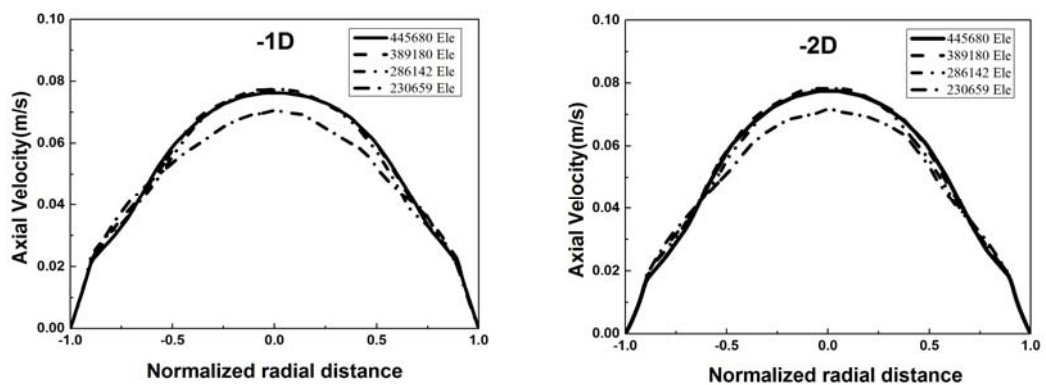


Fig. 7. Axial velocity profiles measured at distances 1D and 2D, before the stenosis region for different grid elements.

3. RESULTS

The demonstration of numerical results emphasizes on multiphase blood flow through idealized straight coronary arteries with different DOS severities. All results were obtained for peak flow at the onset of diastole when the blood velocity reaches maximum at inlet for one cardiac cycle. A detailed numerical analysis of WSS based hemodynamic descriptors distribution such as TAWSS, TAWSSG and OSI over the artery wall has been calculated for different DOS severities.

3.1 Distribution of WSS and WSS based Hemodynamic Descriptors

In various blood flow studies, it has been revealed that distribution of high OSI and low WSS are strongly correlated with the crucial spots of atheroma (He and Ku 1996). Furthermore, the wall permeability is enhanced and atherosclerotic locations spread to sites where the WSS gradients (WSSG) are large (DePaola *et al.* 1992) and amalgamation of high WSS and high exposure times for blood particles can leads to platelets activation (Ramstack *et al.* 1979; Hellums 1994; Hosseinzadegan and Tafti 2017). Hence, in this multiphase non-Newtonian blood flow study, the spatial distributions of WSS based hemodynamic descriptors, including WSS, TAWSS, TAWSSG (Buchanan *et al.* 2003; Ellwein *et al.* 2011; Ryou *et al.* 2012), and OSI (He and Ku 1996), is calculated according to Eq. (29-32), respectively, and compared the same for different DOS severities in idealized human coronary artery.

3.1.1 WSS Distributions in Stenosed Arteries

Figure 8 illustrates the effect of DOS severity on the WSS distributions. Though the peak WSS changes from 0 to several hundreds of Pascal for all the DOS cases it is believed that the neointimal growth risk is higher when the luminal surface subjected to lower WSS than the physiological levels of WSS (<1.5 Pa) (Malek *et al.* 1999; LaDisa *et al.* 2005). Hence, in Fig. 8 WSS is plotted for a range of 0-1.5 Pa in order to study the change in clinically relevant sites for various DOS. Comparing the WSS contour plots between different DOS models in Fig. 8 the

stenosis formation had a noticeable influence on the WSS distributions. Especially large areas of the low WSS endothelial surface are visible in the distal section of the stenosis which is mainly due to low velocity in that region. Also, it is seen that the low WSS (<1.5 Pa) sites in post stenosis region increases for 30% stenosis to 70% stenosis, whereas it decreases for 85% stenosis models.

3.1.2 TAWSS Distributions in Stenosed Arteries

For analyzing the hemodynamics in the artery TAWSS is averaged over one pulsatile cycle. Figure 9 illustrates the effect of DOS severities on the TAWSS distributions. The TAWSS sites where the values are ≥ 10 Pa are shown in red colour. These sites are of clinical relevance as high values of TAWSS (≥ 10 Pa) can lead to the damage of endothelial cells (Suess *et al.* 2016). Hence, in Fig. 9 TAWSS is plotted for a range of 0-10 Pa in order to study the change in clinically relevant sites for various DOS. The low TAWSS is associated with low velocity and subsequently a more likely occurrence of particle immobility. The TAWSS is high (≥ 10 Pa) in the stenosis region for 30% and 50% stenosis models whereas for 70% and 85% stenosis models the TAWSS high (≥ 10 Pa) regions are observed both in stenosis and distal region. Further, as the DOS severity increases TAWSS consistently increases both in stenosis throat and downstream regions.

3.1.3 TAWSSG Distributions in Stenosed Arteries

The TAWSSG is a transient blood flow property, correlated to the wall of the artery. Speedy WSS changes over short distances are measured by the TAWSSG. Figure 10 illustrates the effect of DOS severities on the TAWSSG distributions. The magnitudes of TAWSSG for all stenosis models were ranging from 0 to 200 Pa m⁻¹. The endothelial surface area higher than the physiological levels of TAWSSG (≥ 200 Pa m⁻¹) have been associated to atherosclerotic lesions formation, intimal hyperplasia, and accelerate platelet activation and thrombus formation (DePaola *et al.* 1992; Hosseinzadegan and Tafti 2017). Hence, in Fig. 10

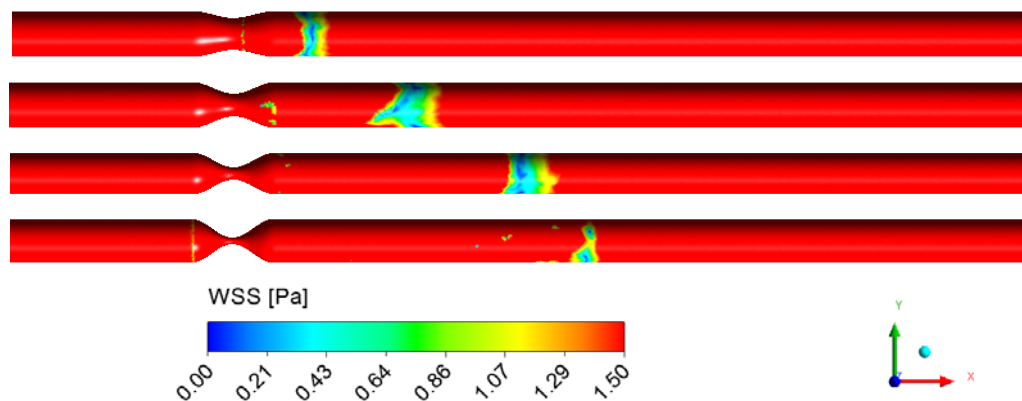


Fig. 8. WSS distributions in idealized coronary artery for different DOS severity models for one cardiac cycle at 0.55s.

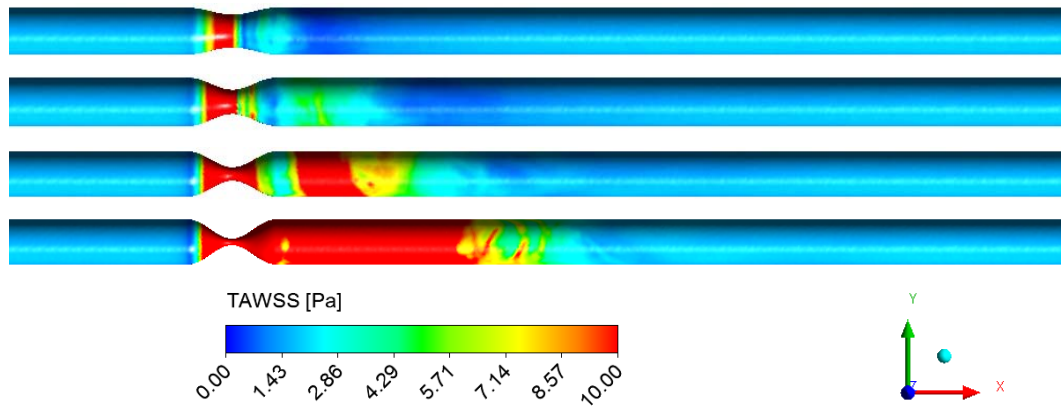


Fig. 9. TAWSS distributions in idealized coronary artery for different DOS severity models averaged over one pulsatile cycle.

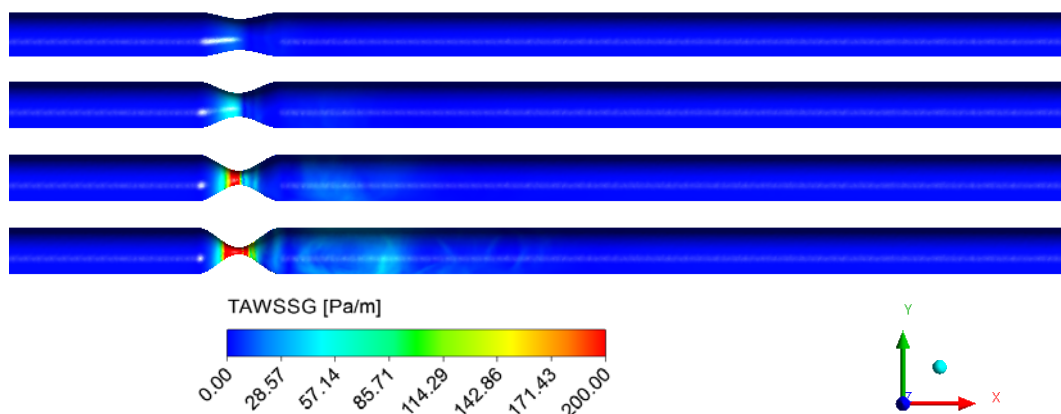


Fig. 10. TAWSSG distributions in idealized coronary artery for different DOS severity models over one cardiac cycle.

TAWSSG is plotted for a range of 0-200 Pa m⁻¹ in order to study the change in clinically relevant sites for various DOS. The large values of TAWSSG (≥ 200 Pa m⁻¹) were observed in the stenosis throat region for 70 and 85% DOS severity models, whereas for the 30 and 50% stenosis models low TAWSSG values ranging from 0 to 57.14 Pa m⁻¹ only was seen.

3.1.4 OSI Distributions in Stenosed Arteries

The OSI is a WSS based dimensionless hemodynamic parameter that provides a measure of the oscillating nature of WSS. Figure 11 depicts the distribution of OSI contours predicted on the artery luminal surface for different DOS severity models over one pulsatile period. It is believed that the neointimal growth risk is higher when the luminal surface endangered to higher OSI than the physiological levels of OSI (>0.3) and hence susceptible to atherogenesis and endothelial dysfunction (Ku *et al.* 1985; Davies 1995; Thury *et al.* 2002). In Fig. 11, OSI contours were plotted for a range of 0-0.3 Pa in order to study the change in clinically relevant sites for various DOS. The higher OSI values were predicted in the distal region of the stenosis and in downstream region of the stenosis for all DOS severity models.

The maximum and average values of WSS and WSS based hemodynamic descriptors and their

percentage increase from the baseline value of 30% DOS were tabulated in Table 2 and 3 respectively. A relatively high positive correlation was observed in maximum and average values of WSS, TAWSS and TAWSSG with DOS and the indicators value increases as the DOS severity increase. However, the OSI indicator is relatively less affected by the DOS.

4. DISCUSSIONS

The present multiphase blood flow study demonstrated that the presence of different DOS severities in coronary arteries produces a synergistic effect on the subsequent WSS and WSS based hemodynamic descriptor's distribution. The variation in the lumen surface area of potential atherosclerotic lesion sites based on WSS, TAWSS, TAWSSG and OSI indicators were studied using their corresponding clinically proven threshold values above or below which endothelial pathological response is induced. The changes in WSS based hemodynamic indicators with respect to DOS were quantified. This is clinically significant as these hemodynamic changes will contribute to further atherosclerotic progress in the coronary artery, leading to potential damage to the arterial wall.

Healthy WSS levels for arteries were reported to vary between 2 to 16 Pa (Cheng *et al.* 2007). The

WSS as low as 1.5 Pa (Malek *et al.* 1999) triggers a biological inflammatory process which leads to the development of atheromatous plaque. From Fig. 11, it is observed that WSS regions having less than 1.5 Pa increases with DOS up to 70% and reduces drastically for 85% DOS. This may be due to the fact that blood flow through 85% stenosis behaves like a strong jet with high velocity after the stenosis and hence high WSS.

For DOS 30% and 50% endothelial surface sites where TAWSS ≥ 10 Pa were found to occur only in the proximal region of stenosis as a result of protuberance of the plaque which leads to the effective flow area reduction (c.f. Fig. 9). The endothelium surface experiencing TAWSS ≥ 10 Pa passes to distal regions of the stenosis for DOS greater than 50%. Hence, damage to endothelial cells in the distal regions likely to occur only when DOS severity increases beyond 50%. Also, higher levels of TAWSS is naturally expected when the fluid flow is maximum i.e., at the cycle systole, where maximum amount of fluid flows through the artery.

In the stenosed artery region as the area of cross section reduces the peak fluid velocity increases.

TAWSSG is a strong function of peak velocity at the center of the artery cross section hence, pathological levels of TAWSSG (>200 Pa m^{-1}) were observed only around the stenosis throat region (Fig. 10). It is interesting to note that adverse clinical outcomes such as intimal hyperplasia and accelerated platelet activation linked with TAWSSG >200 Pa m^{-1} indicator value is likely to occur for DOS $\geq 50\%$ and more likely to occur at the throat than anywhere in the stenosis.

The OSI is used to measure the oscillating nature and the cyclic departure of WSS magnitudes from its main flow direction. The regions with high OSI value experiences severe stretching and compression of endothelial wall which quickens the rupture of plaque and cause sufficient endothelial cells damage. Comparing the OSI contours (Fig. 11), it is clear that the regions of the arterial wall surface subjected to higher physiological value (OSI >0.3) steadily increases with increase in DOS. Also, the length of the artery distal section affected by OSI above 0.3 consistently increases with DOS severity.

The percentage change in maximum and average values of WSS, TAWSS, TAWSSG and OSI with

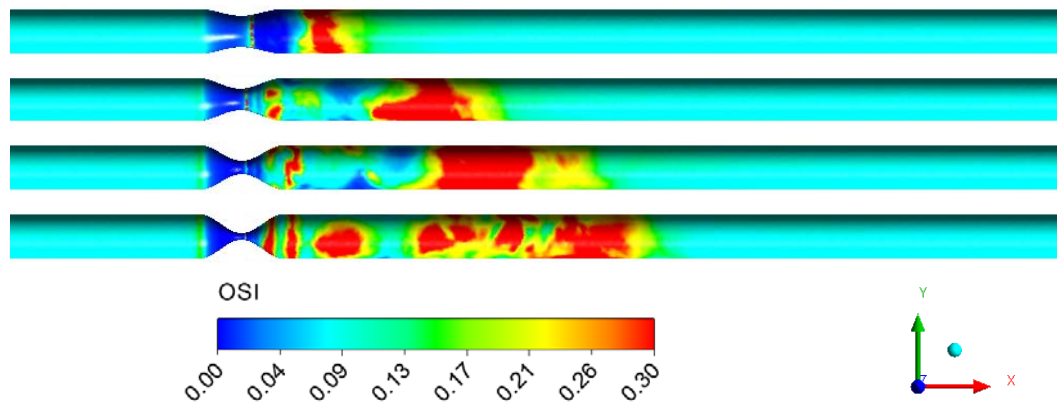


Fig. 11. OSI distributions in idealized coronary artery for different DOS severity models and averaged over one pulsatile cycle.

Table 2 Maximum WSS and WSS based hemodynamic descriptors and their % increase for different DOS severities

| DOS in % | WSS in Pa | | TAWSS in Pa | | TAWSSG in Pam ⁻¹ | | OSI | |
|----------|-----------|------------|-------------|------------|-----------------------------|------------|----------|------------|
| | Max | % Increase | Max | % Increase | Max | % Increase | Max | % Increase |
| 30 | 118.38 | - | 36.65 | - | 36.23 | - | 0.495456 | - |
| 50 | 144.06 | 21.69 | 47.80 | 30.42 | 47.19 | 30.52 | 0.49661 | 0.23 |
| 70 | 881.22 | 644.39 | 283.56 | 673.69 | 281.95 | 678.22 | 0.497788 | 0.47 |
| 85 | 7030.2 | 5838.67 | 2608.01 | 7015.98 | 2597.67 | 7069.94 | 0.495374 | -0.016 |

Table 3 Average WSS and WSS based hemodynamic descriptors and their % increase for different DOS severities

| DOS in % | WSS in Pa | | TAWSS in Pa | | TAWSSG in Pam ⁻¹ | | OSI | |
|----------|-----------|------------|-------------|------------|-----------------------------|------------|---------|------------|
| | Average | % Increase | Average | % Increase | Average | % Increase | Average | % Increase |
| 30 | 4.11 | - | 1.69 | - | 1.43 | - | 0.08758 | - |
| 50 | 4.82 | 17.27 | 1.98 | 17.15 | 1.69 | 18.18 | 0.09571 | 9.28 |
| 70 | 8.33 | 102.67 | 3.25 | 92.30 | 2.78 | 94.40 | 0.10349 | 18.16 |
| 85 | 35.33 | 759.61 | 14.16 | 737.86 | 12.94 | 804.89 | 0.10398 | 18.72 |

respect to DOS is quantified in Table 2 and 3. It is observed that the values increase almost linearly up to DOS 50% and exponentially with DOS beyond 50% DOS. Though potential atherosclerotic sites increase steadily with DOS in general, the increase is exponential with respect to DOS beyond 50%. It is also observed that the maximum value of OSI does not vary with DOS whereas the average value of OSI changes linearly up to 70% DOS and remains unaffected above 70% DOS. This is due to the fact that OSI is strongly dependent on flow pulsatility and turbulence generated. In the present study flow pulsatility is kept constant for all the DOS severities.

4.1 Limitations of the Study

In present study, the idealized coronary artery model with DOS severities were analyzed quantitatively in terms of WSS based hemodynamic descriptors. This model also approaches with an assumption that the blood behaves as a mixture of blood borne particulates and that mixture is considered to be continuum. The present study considers laminar blood flow through a non-compliant artery instead of turbulent flow, as a latest study by Mahalingam *et al.* (Mahalingam *et al.* 2016) showed that in 70% stenosis and above stenosed coronary arteries the blood flow becomes turbulent in nature, whereas, the laminar to turbulent transition of blood flow begins from 50% stenosis.

5. CONCLUSION

In this study, to the best of our knowledge, we have addressed for the first time a multiphase blood flow study using mixture-theory to investigate the WSS and WSS based hemodynamic descriptors in idealized coronary artery for different DOS severities. A hemodynamic model based on mixture theory is utilized to study the transport and interactions of RBCs in the blood plasma. Further, the model was validated with the earlier reported experiments and demonstrated to be more accurate than single phase models. If the stenosis severity is more than 50%, the WSS is very high in stenosis throat and the formation of recirculation zone is higher in post-stenosis region. The plaque rupture risk increases for the DOS above 70% due to very high WSS (> 800 Pa).

It can be concluded that WSS and WSS based hemodynamic indicators were significantly affected by the presence of stenosis and increases with DOS. The values of indicators increase exponentially with DOS above 50% suggesting that the plaque progression rate could be substantially accelerated in the region distal to stenosis for DOS beyond 50%.

This detailed multiphase hemodynamic analysis gives detailed information for deeper understanding of the atherosclerosis formation and plaque progression. Based on the obtained results with the problems studied, we believe that the current multiphase mixture model can be a useful numerical tool for analyzing the blood flow and its transport within the stenosed artery models. Finally, for

clinical usage, the average value of OSI must be used in order to represent the risk instead of maximum values of OSI.

REFERENCES

- Aayani, R., A. Shahidian and M. Ghassemi (2016). Numerical investigation of non-Newtonian blood effect on acoustic streaming. *Journal of Applied Fluid Mechanics* 9(1), 173-176.
- Berne, R. M. and M. N. Levy (1967). *Cardiovascular physiology*. Mosby.
- Berthier, B., R. Bouzerar and C. Legallais (2002). Blood flow patterns in an anatomically realistic coronary vessel: influence of three different reconstruction methods. *Journal of Biomechanics* 35(10), 1347-1356.
- Bronzino, J. D. (1999). *Biomedical engineering handbook*. Vol. 2. CRC press.
- Buchanan, J. R., C. Kleinstreuer, S. Hyun and G. A. Truskey (2003). Hemodynamics simulation and identification of susceptible sites of atherosclerotic lesion formation in a model abdominal aorta. *Journal of Biomechanics* 36(8), 1185-1196.
- Caro, C. G. (2012). *The mechanics of the circulation*. Cambridge University Press, Cambridge, UK.
- Chatzizisis, Y. S., A. U. Coskun, M. Jonas, E. R. Edelman, C. L. Feldman and P. H. Stone (2007). Role of endothelial shear stress in the natural history of coronary atherosclerosis and vascular remodeling: molecular, cellular, and vascular behavior. *Journal of the American College of Cardiology* 49(25), 2379-2393.
- Cheng, C., F. Helderma, D. Tempel, D. Segers, B. Hierck, R. Poelmann, A. van Tol, D. J. Duncker, D. Robbers-Visser, N. T. Ursem and R. van Haperen (2007). Large variations in absolute wall shear stress levels within one species and between species. *Atherosclerosis* 195(2), 225-235.
- Cokelet, G. R. (1987). *The rheology and tube flow of blood*. Handbook of bioengineering, Vol. 14.
- Davies, P. F. (1995). Flow-mediated endothelial mechanotransduction. *Physiological Reviews* 75(3), 519-560.
- DePaola, N., M. A. Gimbrone, P. F. Davies and C. F. Dewey (1992). Vascular endothelium responds to fluid shear stress gradients. *Arteriosclerosis, Thrombosis, and Vascular Biology* 12(11), 1254-1257.
- Egorov, V. A., S. A. Regirer and N. K. Shadrina (1994). Properties of pulsating blood flow through resistive blood vessels. *Fluid Dynamics* 29(2), 221-226.
- Ellwein, L. M., H. Otake, T. J. Gundert, B. K. Koo, T. Shinke, Y. Honda, J. Shite and J. F. LaDisa (2011). Optical coherence tomography for patient-specific 3D artery reconstruction and

- evaluation of wall shear stress in a left circumflex coronary artery. *Cardiovascular Engineering and Technology* 2(3), 212-227.
- Gidaspow, D. (1994). *Multiphase flow and fluidization: continuum and kinetic theory descriptions*. Academic press. Cambridge, Massachusetts, US.
- Gijssen, F. J., F. N. van de Vosse and J. D. Janssen (1999). The influence of the non-Newtonian properties of blood on the flow in large arteries: steady flow in a carotid bifurcation model. *Journal of Biomechanics* 32 (6), 601-608.
- Hasan, A. B. M. and D. K. Das (2008). Numerical simulation of sinusoidal fluctuated pulsatile laminar flow through stenotic artery. *Journal of Applied Fluid Mechanics* 1(2), 25-35.
- Haynes, R. H. (1960). Physical basis of the dependence of blood viscosity on tube radius. *American Journal of Physiology-Legacy Content* 198(6), 1193-1200.
- He, X. and D. N. Ku (1996). Pulsatile flow in the human left coronary artery bifurcation: average conditions. *Journal of Biomechanical Engineering* 118(1), 74-82.
- Hellums, J. D. (1994). 1993 Whitaker Lecture: biorheology in thrombosis research. *Annals of Biomedical Engineering* 22(5), 445-455.
- Hoi, Y., H. Meng, S. H. Woodward, B. R. Bendok, R. A. Hanel, L. R. Guterman and L. N. Hopkins (2004). Effects of arterial geometry on aneurysm growth: three-dimensional computational fluid dynamics study. *Journal of Neurosurgery* 101(4), 676-681.
- Hosseinzadegan, H. and D. K. Tafti (2017). Prediction of thrombus growth: effect of stenosis and Reynolds number. *Cardiovascular Engineering and Technology* 8(2), 164-181.
- Ishii, M. and T. Hibiki (2010). *Thermo-fluid dynamics of two-phase flow*. Springer Science & Business Media, Berlin, Germany.
- Kizilova, N. N., S. A. Logvenkov and A. A. Stein (2012). Mathematical modeling of transport-growth processes in multiphase biological continua. *Fluid Dynamics* 47(1), 1-9.
- Ku, D. N., D. P. Giddens, C. K. Zarins and S. Glagov (1985). Pulsatile flow and atherosclerosis in the human carotid bifurcation. Positive correlation between plaque location and low oscillating shear stress. *Arteriosclerosis, Thrombosis, and Vascular Biology* 5(3), 293-302.
- LaDisa Jr, J. F., L. E. Olson, R. C. Molthen, D. A. Hettrick, P. F. Pratt, M. D. Hardel, J. R. Kersten, D. C. Wartier and P. S. Pagel (2005). Alterations in wall shear stress predict sites of neointimal hyperplasia after stent implantation in rabbit iliac arteries. *American Journal of Physiology-Heart and Circulatory Physiology* 288(5), H2465-H2475.
- Li, G., R. Hu and F. Gao (2015). Numerical simulation of coronary artery stenosis before and after stenting. *Journal of Medical and Biological Engineering* 35(4), 528-534.
- Lowe, G. D. O., F. G. R. Fowkes, J. Dawes, P. T. Donnan, S. E. Lennie and E. Housley (1993). Blood viscosity, fibrinogen, and activation of coagulation and leukocytes in peripheral arterial disease and the normal population in the Edinburgh Artery Study. *Circulation* 87(6), 1915-1920.
- Mahalingam, A., U. U. Gawandalkar, G. Kini, A. Buradi, T. Araki, N. Ikeda, A. Nicolaides, J. R. Laird, L. Saba and J. S. Suri (2016). Numerical analysis of the effect of turbulence transition on the hemodynamic parameters in human coronary arteries. *Cardiovascular Diagnosis and Therapy* 6(3), 208-220.
- Malek, A. M., S. L. Alper and S. Izumo (1999). Hemodynamic shear stress and its role in atherosclerosis. *The Journal of the American Medical Association* 282(21), 2035-2042.
- Manninen, M., V. Taivassalo and S. Kallio (1996). *On the mixture model for multiphase flow*, VTT Publications 288, Technical Research Centre of Finland.
- Massoudi, M. (2002). On the importance of material frame-indifference and lift forces in multiphase flows. *Chemical Engineering Science* 57(17), 3687-3701.
- Mesri, Y., H. Niazmand and A. Deyranlou (2017). Numerical study on fluid-structure interaction in a patient-specific abdominal aortic aneurysm for evaluating wall heterogeneity and material model effects on its rupture. *Journal of Applied Fluid Mechanics* 10(6), 1699-1709.
- Nichols, W. W. and M. F. O'Rourke (2005). *McDonald's blood flow in arteries: theoretical, experimental and clinical principles*, Vol. 340809418, London: Hodder Arnold.
- Nosovitsky, V. A., O. J. Ilegbusi, J. Jiang, P. H. Stone and C. L. Feldman (1997). Effects of curvature and stenosis-like narrowing on wall shear stress in a coronary artery model with phasic flow. *Computers and Biomedical Research* 30(1), 61-82.
- Oka, S. (1981). *Cardiovascular hemorheology*. CUP Archive, Cambridge, UK.
- Patrick, M. J., C. Y. Chen, D. H. Frakes, O. Dur and K. Pekkan (2011). Cellular-level near-wall unsteadiness of high-hematocrit erythrocyte flow using confocal μ PIV. *Experiments in Fluids* 50(4), 887-904.
- Quemada, D. (1981). A rheological model for studying the hematocrit dependence of red cell-red cell and red cell-protein interactions in blood. *Biorheology* 18(3-6), 501-516.
- Quemada, D. (1977). Rheology of concentrated disperse systems and minimum energy dissipation principle. *Rheologica Acta* 16(1), 82-94.

- Quemada, D. (1978). Rheology of concentrated disperse systems II. A model for non-Newtonian shear viscosity in steady flows. *Rheologica Acta* 17(6), 632-642.
- Rajagopal, K. R., W. Troy and M. Massoudi (1992). Existence of solutions to the equations governing the flow of granular materials. *European Journal of Mechanics* 11(3), 265-276.
- Ramstack, J. M., L. Zuckerman and L. F. Mockros (1979). Shear-induced activation of platelets. *Journal of Biomechanics* 12(2), 113-125.
- Razavi, A., E. Shirani and M. R. Sadeghi (2011). Numerical simulation of blood pulsatile flow in a stenosed carotid artery using different rheological models. *Journal of Biomechanics* 44(11), 2021-2030.
- Reinke, W., P. Gaehtgens and P. C. Johnson (1987). Blood viscosity in small tubes: effect of shear rate, aggregation, and sedimentation. *American Journal of Physiology-Heart and Circulatory Physiology* 253(3), H540-H547.
- Ren, X., A. Qiao, H. Song, G. Song and L. Jiao (2016). Influence of bifurcation angle on in-stent restenosis at the vertebral artery origin: A simulation study of hemodynamics. *Journal of Medical and Biological Engineering* 36(4), 555-562.
- Ryou, H. S., S. Kim, S. W. Kim and S. W. Cho (2012). Construction of healthy arteries using computed tomography and virtual histology intravascular ultrasound. *Journal of Biomechanics* 45(9), 1612-1618.
- Stadler, A. A., E. P. Zilow and O. Linderkamp (1990). Blood viscosity and optimal hematocrit in narrow tubes. *Biorheology* 27(5), 779-788.
- Steinman, D. A. (2002). Image-based computational fluid dynamics modeling in realistic arterial geometries. *Annals of Biomedical Engineering* 30(4), 483-497.
- Suess, T., J. Anderson, L. Danielson, K. Pohlson, T. Remund, E. Blears, S. Gent and P. Kelly (2016). Examination of near-wall hemodynamic parameters in the renal bridging stent of various stent graft configurations for repairing visceral branched aortic aneurysms. *Journal of Vascular Surgery* 64(3), 788-796.
- Thury, A., J. J. Wentzel, R. V. Vinke, F. J. Gijssen, J. C. Schuurbiers, R. Krams, P. J. de Feyter, P. W. Serruys and C. J. Slager (2002). Focal in-stent restenosis near step-up. *Circulation* 105(23), e185-e187.
- Yan, F., W. T. Jiang, R. Q. Dong, Q. Y. Wang, Y. B. Fan and M. Zhang (2017). Blood flow and oxygen transport in descending branch of lateral femoral circumflex arteries after transfemoral amputation: A numerical study. *Journal of Medical and Biological Engineering* 37(1), 63-73.
- Zeng, D., Z. Ding, M. H. Friedman and C. R. Ethier (2003). Effects of cardiac motion on right coronary artery hemodynamics. *Annals of Biomedical Engineering* 31(4), 420-429.
- Zhang, J. M., L. P. Chua, D. N. Ghista, S. C. M. Yu and Y. S. Tan (2008). Numerical investigation and identification of susceptible sites of atherosclerotic lesion formation in a complete coronary artery bypass model. *Medical & Biological Engineering & Computing* 46(7), 689-699.